Journal of Physics: Materials

PAPER

Conductive metal-organic framework synthesis from metal nanoparticle precursors

Abigail M Lister*, **Yu Wang**, **Ben I Armitage**, **Weishuo Li** and **Martin R Castell***

Department of Materials, University of Oxford, Parks Road, Oxford OX1 3PH, United Kingdom
* Authors to whom any correspondence should be addressed.

E-mail: abigail.lister@materials.ox.ac.uk and martin.castell@materials.ox.ac.uk

Keywords: conducting MOF, metal nanoparticle, chemical synthesis

Supplementary material for this article is available online

OPEN ACCESS

RECEIVED
5 September 2024

REVISED
1 January 2025

ACCEPTED FOR PUBLICATION
6 February 2025

PUBLISHED
19 February 2025

Abstract

Conductive metal-organic frameworks (MOFs) have potential applications as critical functional materials in electronic devices such as chemiresistive sensors, capacitors and batteries. However, the widespread adoption of MOFs in devices is limited by the lack of reliable methods to generate uniform distributions of the MOFs *in situ* that are strongly adhered to the desired substrates. Here we present a method of synthesising electrically conductive $Cu_3(HITP)_2$ and $Ni_3(HITP)_2$ MOFs from Cu and Ni metal nanoparticles. The metal nanoparticles are deposited from a magnetron plasma sputtering source onto substrates that include cotton, glass, gold and paper. These nanoparticle-decorated substrates are then immersed in a mildly alkaline solution of the ligand in the presence of an electrolyte. This results in the growth of MOF on the substrate only where the metal nanoparticles were deposited. The described method overcomes problems associated with drop-casting suspensions of the conductive MOF by generating uniform distributions *in situ* on the substrates. Both MOFs were generated successfully on all four of the substrates, with no preference for conducting or insulating substrates. The mild chemical synthesis environment and proven success with a variety of substrates indicate that the method is likely to be of wide applicability.

1. Introduction

Metal-organic frameworks (MOFs) are attractive materials for use in a variety of settings due to their porosity and tuneable chemical and physical functionalities. These include environmental applications such as carbon capture [1–4], water purification [5–7] and energy storage [8–10]. In addition, MOF-derived catalysts have been employed for water splitting [11, 12], and in battery electrodes [13, 14]. By changing the constituent metal nodes and organic linkers, MOFs can be designed to perform particular functions [15]. The dimensionality of the framework can be altered by manipulating the denticity of the organic linkers. For example, hexadentate triphenylene-based ligands enable the formation of 2D MOF sheets [16]. The geometry of the resulting MOFs is such that the metal d-orbitals effectively overlap with the π system of the ligand to result in extended charge delocalisation and thus an intrinsically electrically conductive MOF. The discovery of conductive MOFs by Yaghi and co-workers [16] has enabled MOFs to be considered for a broad range of applications including chemiresistive sensing [17–20], electrocatalysis [21–23], and electrochemical energy storage [24–26].

Powders of 2D conductive MOFs can be synthesised through hydrothermal [16], microwave-assisted [27], and ultrasonic [28] methods, but further processing is required to integrate the resulting powders into electronic devices. Dispersion in solution followed by drop-casting was the first approach adopted to deposit MOF onto the interdigitated electrodes (IDEs) used for impedimetric gas sensing [29]. However, drop-cast MOF systems often suffer from inhomogeneous distribution, poor conductivities due to high contact resistance, and poor substrate adhesion. Alternatives to drop casting have been investigated including mechanical abrasion [17], spray-coating [30], spin-coating [31] and surface-assisted methods such as application of the Langmuir Blodgett technique [32]. *In situ* synthesis routes can eliminate the need to

deposit MOFs onto the desired substrates entirely[33]. One such method is the spray layer-by-layer synthesis method reported by Yao *et al* in which substrates are in-turn sprayed by solutions of ligand and metal salt to obtain the MOF [34]. This was successful on silicon, quartz and sapphire substrates, but as piranha solution is needed to functionalise the substrates this method cannot be used to obtain MOF on flexible substrates such as PET, paper and textiles.

Methods that produce conducting MOFs on insulating flexible substrates are desirable for use in wearable electronic devices such as chemiresistive gas sensors [35], electrochemical glucose monitors [36] and pressure sensors [37]. This has driven demand for straightforward methods of generating conductive MOFs on a variety of substrates. *In situ* growth methods such as the electrochemical synthesis of MOFs are promising in terms of substrate adhesion, MOF homogeneity and morphological control. However, these methods are limited to MOF formation on metal anodes and the steps required to remove the MOF from the anodes and re-adhere them to insulating substrates are lengthy and complex [38–40]. Subsequent reports describe how the conductive MOF $Cu_3(HHTP)_2$ can be synthesised directly on fabric by coating fibres in copper nanoparticles and then exposing them to solutions of the HHTP ligand [41, 42]. The first of these methods involves converting the nanoparticles to $Cu(OH)_2$ nanowires using a concentrated sodium hydroxide and ammonium persulphate solution, before submerging the substrates in a DMF/H_2O ligand solution at an elevated temperature over a period of hours. Similar work describes how copper nanoparticles deposited on a variety of woven substrates can be converted into $Cu_3(HHTP)_2$ MOF by submerging the substrates in a neutral ligand solution. H_2O_2 gas bubbling was required to reduce the synthesis time from 12 h to 15 min [42]. The resulting MOF was used as an effective gas sensor for NO and H_2S gases [42].

Here, we present a method to synthesise two triphenylene-based MOFs, $Cu_3(HITP)_2$ and $Ni_3(HITP)_2$, *in situ* on glass, gold, paper and cotton substrates. The method involves direct synthesis of the MOFs from nanoparticles of the relevant metal. The nanoparticles are deposited on the desired substrate and the MOF is formed when the substrate is submerged in weakly alkaline solutions of the ligand. The syntheses take place within one hour, at room temperature and no harsh solvents are required. The MOF grows outwards from the deposited nanoparticles, and hence the resulting MOF coverage reflects the uniform distribution of the nanoparticles. As the synthesis occurs directly from the metal nanoparticles, the advantages typical of salt-free synthetic methods, such as minimising the formation of unwanted byproducts, are also retained. We observe good adhesion of the MOF to the tested substrates and the mild solution conditions mean that this method is likely to be scalable for use for MOF formation on the majority of substrates used in electronic devices or for MOF-functionalised materials.

The two MOFs to which our synthesis method is applied are based on the triphenylene linker 2,3,6,7,10,11-hexaiminotriphenylene (HITP, which is the hexa-dehydrogenated imine form of HATP) combined with either Cu or Ni metal nodes. The resulting MOFs, $Cu_3(HITP)_2$ and $Ni_3(HITP)_2$, are both comprised of 2D hexagonal sheets (figure 1) which stack in a slipped parallel arrangement to create extended pores throughout the crystal [16, 43]. Because of their inherent conductivity, these MOFs have been investigated as the active material for use in a variety of devices [44]. For example, Dinca *et al* report using these MOFs to form a chemiresistive sensing array able to distinguish between different classes and concentrations of volatile organic compounds [17], whilst Miner *et al* describe how $Ni_3(HITP)_2$ can be used as a catalyst for oxygen reduction [45]. The numerous potential uses of these MOFs means that improved synthesis routes are of significant interest.

2. Materials and methods

2.1. Materials synthesis

Cu and Ni nanoparticles were deposited onto the substrates using a dc magnetron plasma sputtering source (NL50, Nikalyte Ltd.). Four different substrates were used: Pt IDEs with 5 μm gap sizes on glass (Micrux Technologies, Spain), white paper card (WHSmith, UK), 200 thread count cotton percale (Dalston Mill Fabrics, UK) and 300 nm Au (111) films on mica (Georg Albert PVD, Germany). Cu or Ni nanoparticles were deposited on to the four substrates: 7000 ng cm^{-2} on Au(111), 8000 ng cm^{-2} on cotton, 5000 ng cm^{-2} on paper, and 7000 ng cm^{-2} on the Pt IDEs. We note that 1000 ng cm^{-2} corresponds to around 1.1 nm layer thickness for a continuous Ni or Cu film equivalent. The nanoparticles were observed to have diameters between 10 and 50 nm. The fabric and paper nanoparticle-decorated substrates had infinite resistances when measured with a multimeter across 5 mm of the sample, indicating that a continuous thin film has not formed. Similarly, the measured resistances across the IDEs after nanoparticle deposition are of the order of hundreds of kΩ indicating that some of the nanoparticles must be touching sufficiently to form some conductive pathways across the 5 μm gaps in the IDEs. Each nanoparticle-decorated substrate was then submerged in a vial containing a 2 mM solution of the HATP·6HCl ligand (2,3,6,7,10,11-hexaaminotriphenylene hexachloride, 97%, BLD Pharmatech, Germany) in 4 ml of ethanol and 1 ml of

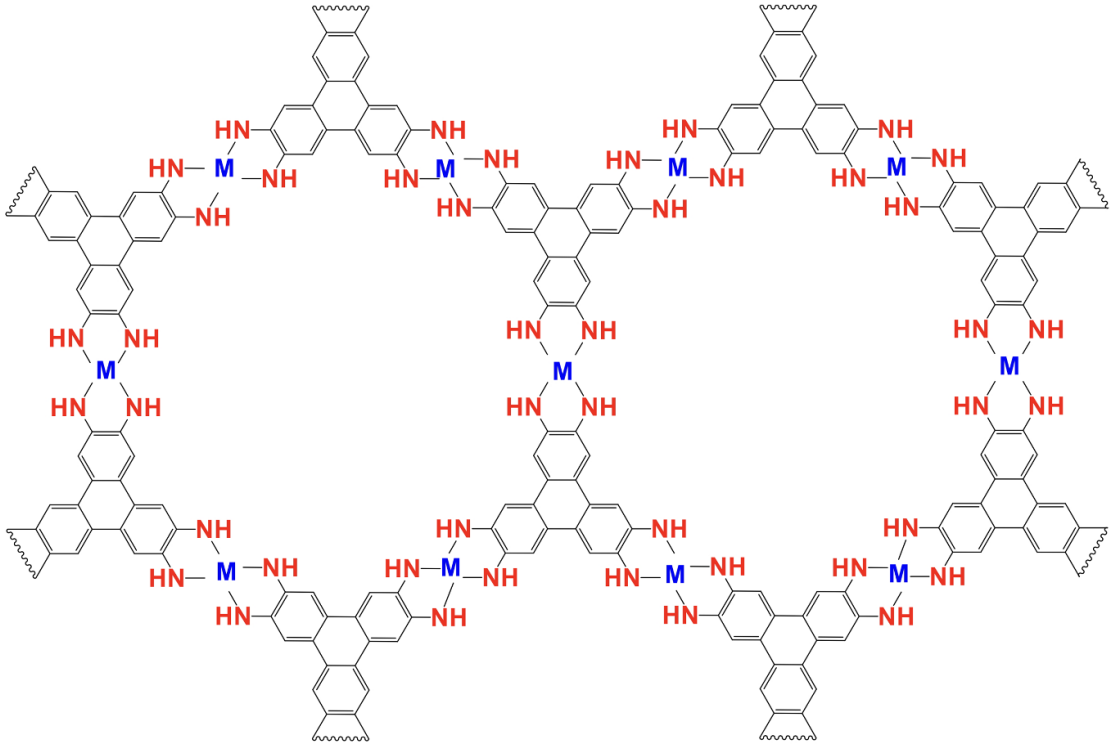

Figure 1. Schematic representation of a single layer of $Cu_3(HITP)_2$ and $Ni_3(HITP)_2$ MOF. The metal (M) is either Cu or Ni. Layers of this MOF stack to form 3D structures with pore channels.

water. To each vial, 375 μl of 19.4 M ammonia solution (Fisher Scientific UK), and 0.10 mmol of tributylmethylammonium methyl sulphate (TBMAMS, 97%, Santa Cruz Biotechnology, USA) were added (figure 2). Substrates were left in the ligand solutions for a set amount of time between 1 min and 24 h, after which the solution was pipetted off and the substrate left to dry at room temperature in air overnight.

The schematic in figure 2 shows the reaction of the high surface-area metal nanoparticles with the HATP ligand solution which eventually leads to $M_3(HITP)_2$ MOF formation around the nanoparticles. The proposed growth mechanism involves the reaction of the hydroxide ions in the solution with the native metal oxide surface layer of the nanoparticles. This will result in a layer of metal hydroxide $M(OH)_2$ on the surface of the nanoparticles. In parallel, the hydroxide ions also deprotonate one of the two amine groups on each arm of the HATP leading to the partial imine form of the deprotonated molecule. Subsequent oxidation of this molecule by dissolved oxygen in the solution results in a partial imine radical which in turn reacts with the hydroxide ions causing deprotonation that leads to the hexaimine form ($HITP^{3-}$). This is the activated form of the ligand that can react with the metal ions to form the MOF.

The growth of the MOF can occur at two main locations: the interface between the metal hydroxide on the surface of the nanoparticles (interface growth), or on the surface of the MOF (surface growth). For interface growth the activated ligands diffuse through the MOF to the nanoparticle surface and react with the surface metal hydroxide:

$$2\,\mathrm{HITP}^{3-} + 3\mathrm{M(OH)_2} \rightarrow \mathrm{M_3(HITP)_2} + 6\,\mathrm{OH}^-.$$

Alternatively, surface growth involves the dissolution of the metal hydroxide to release M^{2+} ions around the nanoparticles, which then diffuse through the MOF. Once the M^{2+} ions reach the surface of the MOF they react with the activated HITP to perpetuate growth:

$$\mathrm{M(OH)_2} \leftrightarrows \mathrm{M}^{2+} + 2\,\mathrm{OH}^-$$

$$2\,\mathrm{HITP}^{3-} + 3\,\mathrm{M}^{2+} \rightarrow \mathrm{M_3(HITP)_2}.$$

For both growth modes the metal in the nanoparticles is consumed as the MOF grows. The MOF is anchored to the nanoparticles acting as the metal source, which in turn are anchored to the substrate on which they were deposited. The faster growth rate of $Cu_3(HITP)_2$ compared to $Ni_3(HITP)_2$ may be due to the higher solubility of $Cu(OH)_2$ (39.8 g l^{-1}) versus $Ni(OH)_2$ (0.13 g l^{-1}) in water at 20 °C.

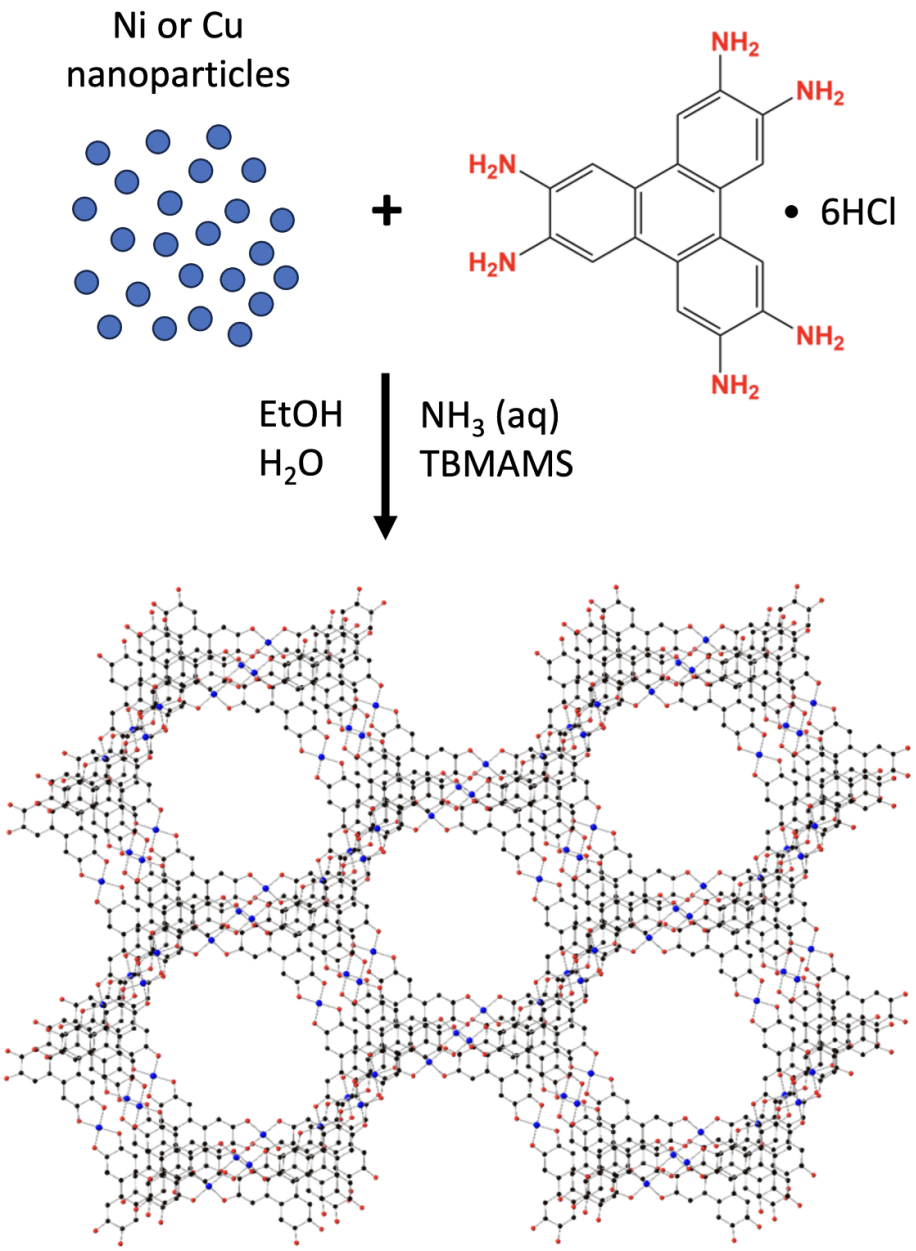

Figure 2. Reaction scheme for formation of the $Cu_3(HITP)_2$ and $Ni_3(HITP)_2$ MOFs from Ni or Cu nanoparticles. The metal nanoparticles react with the HATP ligand (top right) in an ethanol/water solvent in the presence of TBMAMS electrolyte and NH_3(aq). The products are hexagonal $M_3(HITP)_2$ MOF sheets that stack with slipped parallel stacking to form 3D crystals with pore channels (bottom).

Numerous experiments were performed in which the amounts of ligand, electrolyte (TBMAMS) and ammonia solution were modulated (further information is presented in the supplementary information). Syntheses attempted in the absence of electrolyte resulted in the formation of large (8 μm edge length) triangular crystals and significantly less MOF (figure S20), with energy dispersive x-ray (EDX) analysis suggesting that these features are crystalline forms of the HATP ligand, after removal of the coordinated HCl. Through adding the TBMAMS, formation of these crystals is inhibited, confirming the key role that the TBMAMS plays in the reaction in stabilising the soluble form of the HATP ligand. This stabilisation is suspected to occur by increasing the concentration of counter ions that can react with excess ammonium hydroxide, without acting to interfere with the MOF growth. This is further discussed in the supplementary information.

2.2. Characterisation techniques

X-ray photoelectron spectroscopy (XPS), Raman spectroscopy, powder x-ray diffraction (PXRD), transmission electron microscopy (TEM), and scanning electron microscopy (SEM) in combination with EDX analysis were used for sample characterisation. For XPS a K-alpha instrument from Thermo Scientific,

UK was used. Raman spectroscopy was carried out with a System 1000 instrument from Renishaw, UK. Scans were performed over a range of 500–2500 cm^{-1}, with an acquisition time of 40 s. The PXRD instrument used was a Miniflex from Rigaku, Japan with a 1.54 Å Cu Kα x-ray source. The sample was scanned from 2° to 50° at a rate of 5° min^{-1} with a step size of 0.02°. SEM images were taken on an analytical Merlin instrument from Zeiss, Germany. To image the MOF on Au and MOF on IDE samples, conductive tape was used to ensure electrical connection between the conductive top surfaces of the samples and the SEM sample holder. For the MOF on cotton and paper samples, silver dag contacts were drawn on to the substrates, to which conductive tape was connected to ensure charge could flow between the MOF and the SEM holder. Accelerating voltages between 3 kV and 6 kV were used for imaging with a probe current of 100 pA. Secondary electron images were taken with the InLens detector. The same instrument was used for EDX experiments, with an accelerating voltage of 6 kV. TEM was carried out on a JEM-2100 instrument from JEOL, Japan operating at 200 kV. TEM samples were prepared from MOF made via submersion of pure bulk metal in the alkaline ligand and electrolyte solution. The MOF was scraped off the surface of the metal, dispersed in ethanol and then drop-cast onto Cu TEM grids with a holey carbon film.

3. Results and discussion

Evidence of MOF forming from the nanoparticles can be observed at the microscopic and macroscopic levels. By eye, the colour of the nanoparticle-decorated substrates can be observed to darken as the grey nanoparticles are consumed and the black MOF forms. This is shown in figure S1 in the SI where Cu and Ni nanoparticle-decorated paper substrates are immersed for varying amounts of time in the alkaline ligand and electrolyte solution. Changes in the morphology of the MOF are explored using SEM as shown in subsequent sections.

For the $Cu_3(HITP)_2$ and $Ni_3(HITP)_2$ MOFs formed on the glass IDEs, XPS and Raman spectroscopy were carried out with the MOFs still adhered to the substrate. The XPS survey scans depicted in figures 3(a) and (b) show the presence of the constituent MOF elements and are consistent with previously reported XPS spectra for these MOFs [46, 47]. Survey scans of the same MOFs synthesised on the fabric, paper and Au substrates also indicate the presence of the expected MOF elements [$Cu_3(HITP)_2$: figures S6–S9; $Ni_3(HITP)_2$: figures S14–S16]. Closer analysis of the Ni and Cu regions provide an insight into the oxidation states of the metals [$Cu_3(HITP)_2$: figures S10–S13; $Ni_3(HITP)_2$: figures S17–S19]. The binding energies for the Ni $2p_{3/2}$ sub-shells are above 855.5 eV for MOF synthesised on all of the substrates. The absence of metal peaks at lower binding energies indicates a complete conversion of Ni to the Ni^{2+} species within the 6 nm inelastic mean free path lengths of the electrons (figures S17–S19). Narrow area scans of the Cu 2p regions for the Cu MOFs on different substrates (figures S10–S13) show satellites for both the $2p_{3/2}$ and $2p_{1/2}$ peaks, indicating that Cu^{2+} ions are present. Peaks consistent with Cu/Cu^{+} species are also present. As the binding energies for metallic Cu and Cu^{+} are coincident for copper compounds, it cannot be ruled out that residual copper remains within the nanoparticles for the $Cu_3(HITP)_2$ MOF. *In situ* PXRD experiments would be required to determine whether any elemental Cu or Ni nanoparticle cores remain. The Raman spectra depicted in figure 3(c) show the presence of peaks in the MOF spectra that are not observed in the spectrum for the HATP ligand on its own, demonstrating that a chemical transformation has indeed occurred on the surface of the substrates.

The thickness of the MOF layers relative to the substrates' roughness meant that PXRD experiments could not be carried out with the MOF still on the substrates using the available equipment. In the case of the $Cu_3(HITP)_2$ MOF, the synthesis was scaled up using copper foil instead of nanoparticles for the purposes of PXRD. Enough MOF was produced in this experiment so that the powder could be scraped off the foil and PXRD data could be obtained (figure 3(d)). Peaks were observed at $2\theta = 4.7°$, 9.6°, 12.6°, 16.6° and 27.4° which are consistent with the peak positions reported in literature [48]. When indexed according to a hexagonal unit cell, these peaks correspond to lattice parameters of $a = b = 21.7$ Å and $c = 3.2$ Å. The (001) peak at $2\theta = 27.5°$ is however significantly sharper than typically reported, suggesting enhanced long range order in the interlayer c-direction for MOFs created via this synthesis method. The two additional starred peaks at $2\theta = 35.6°$ and 38.6° can be assigned to CuO crystals [49]. The CuO is presumed to form from the $Cu(OH)_2$ intermediate as the foil dries after removal from solution. The small peak at around 24° cannot be assigned to any reflections in the MOF, starting materials or any likely side products. It is therefore assumed to be due to trace metal impurities in the Cu foil (99.98%) used for this scaled up synthesis, or impurities in the HATP ligand (97%) or the TBMAMS electrolyte (97%). Unfortunately not enough material could be produced to obtain PXRD data for the $Ni_3(HITP)_2$ MOF. TEM was therefore carried out in order to determine the lattice structure of both MOFs. MOF powder synthesised from pure Ni and Cu metal was scraped off the metal surfaces and deposited onto TEM grids. In both cases, stacks of the 2D MOF sheets were visible and the interlayer spacing could be measured. For the Cu MOF (figure 4(a)), the spacing was

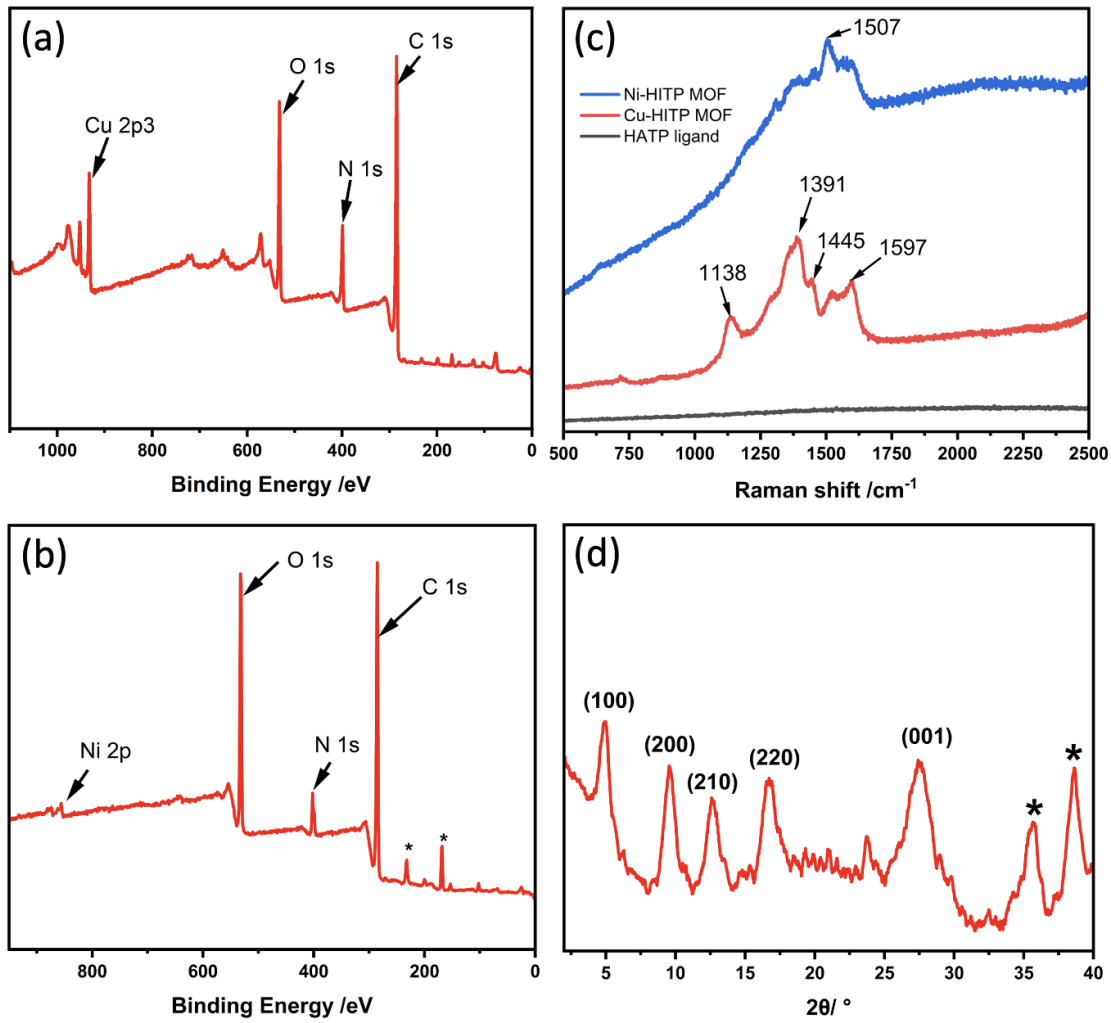

Figure 3. (a) XPS survey scan for the $Cu_3(HITP)_2$ MOF on glass interdigitated electrode substrate. (b) XPS survey scan for the $Ni_3(HITP)_2$ MOF on glass interdigitated electrode substrate. The starred peaks are due to residual sulphur. (c) Raman spectra for $Cu_3(HITP)_2$ MOF (red) and $Ni_3(HITP)_2$ MOF (blue) synthesised *in situ* on glass interdigitated electrodes. The HATP ligand is also shown (grey) but there are no distinctive features. (d) Powder X-ray diffraction scan for $Cu_3(HITP)_2$ synthesised on copper foil. The MOF reflections are indexed. The two starred peaks are due to CuO crystals.

measured to be 3.2 Å, which is consistent with the lattice parameter *c* ascertained from the PXRD results. For the Ni MOF (figure 4(b)), the interlayer spacing was measured to be 3.3 Å, which is also consistent with the literature-reported value [43].

For the copper nanoparticles deposited on paper, SEM images show how the $Cu_3(HITP)_2$ MOF growth initiates from the nanoparticles within 10 min of submersion in the synthesis solution, with the smaller particles growing and aggregating to form bigger features as the synthesis time increases (figure 5). At 0 min the nanoparticles can be seen as spot-like features covering the paper substrate. After 10 min these features have noticeably grown outwards from the paper substrate. After 1 h, larger rounded features formed from the amalgamation of smaller MOF crystallites are observed on top of the paper. In the lower magnification image, we observe that the number of larger amalgamated crystallites is sufficient for connected MOF crystallites to bridge the paper fibres in multiple places. Treating a series of Ni nanoparticles on paper with the synthesis solution for the same series of times enables the growth rate of $Ni_3(HITP)_2$ to be compared to that of $Cu_3(HITP)_2$. A likely growth mechanism is that larger amalgamated MOF crystallites start to form on top of the paper fibre surfaces once the MOF particles have grown sufficiently to completely cover the fibre. We can estimate the time taken for growth to this completely covered state by observing the time at which the larger amalgamated crystallites start to grow. By comparing the time series SEM images for $Cu_3(HITP)_2$ and $Ni_3(HITP)_2$ in figures S2 and S3, respectively, it can be observed that these larger MOF features are observed within the first 10 min for the Cu MOF, but not until a time between 1 h and 2 h for the Ni MOF. This allows us to estimate the rate of growth of the Cu MOF to be a minimum of 6 times faster than that of the Ni MOF in this experiment.

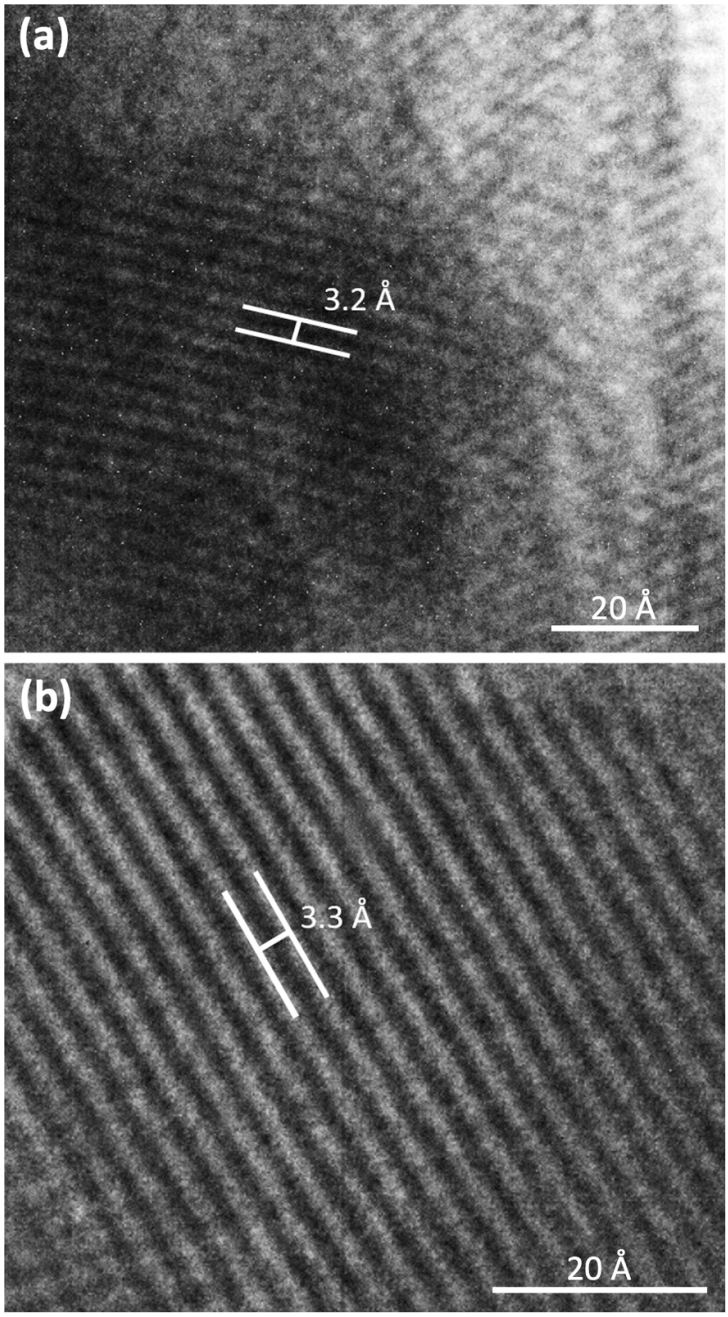

Figure 4. (a) TEM image depicting the 3.2 Å interlayer spacing in $Cu_3(HITP)_2$ MOF. (b) TEM image depicting the 3.3 Å interlayer spacing in $Ni_3(HITP)_2$ MOF.

SEM images of the same $Cu_3(HITP)_2$ MOF formed by submerging nanoparticles on cotton, Au(111) and Pt/glass IDE into the synthesis solution for 1 h can be seen in figure 6. Features larger than the initial nanoparticles are observed to form on all of the substrates, supporting the proposal that the MOF grows out from the nanoparticles. Some larger features assumed to be amalgamated MOF crystallites are also visible on top of the substrates. For the glass and gold substrates, the MOF particles appear evenly distributed across the flat surface of the substrate, whilst they follow the curved surface of the fibres present in the paper and cotton samples. SEM imaging reveals that similar structures form for the case of $Ni_3(HITP)_2$ MOF on the same substrates (figure S5). Consistent with the time-point experiments performed on paper substrates, the broadening of the Ni nanoparticle features is less pronounced within 1 h across all of the substrates, reflective of the slower growth rate of the Ni MOF. As expected, there are fewer larger features that can be attributed to amalgamated crystallites across the paper, gold and glass samples than are present in the copper samples. The

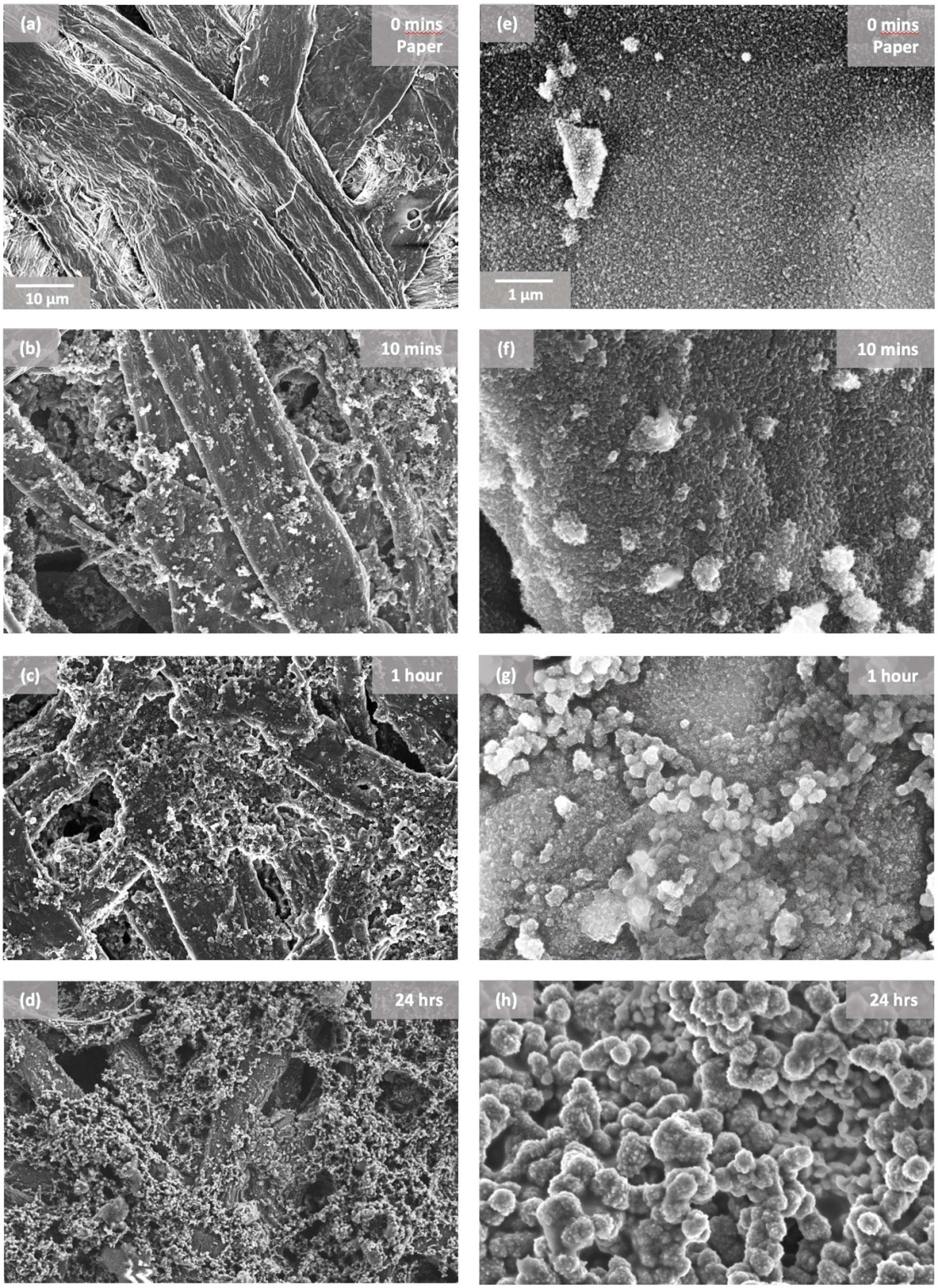

Figure 5. SEM images of Cu nanoparticles deposited on paper after different submersion times in the ligand synthesis solution. The submersion time is noted in the top right of each image. The top row depicts only nanoparticles, whereas $Cu_3(HITP)_2$ MOF is visible for the samples submerged in the ligand solution for 10 mins, 1 h and 24 h. Each row depicts the same sample imaged at two different magnifications (10 μm scale bar applies to the left column, 1 μm scale bar to the right column.).

fabric sample however, shows a surprisingly high concentration of amalgamated crystallites in the imaged region. This is likely due to the fibrous and rough nature of the substrate, whereby nanoparticles deposited in between fibres or on the sides of the fibres will be adhered less strongly to the substrate and so form MOF crystallites that can more readily amalgamate.

The slower growth rate of the Ni MOF compared to the Cu MOF on paper is corroborated in figure 7, which depicts Ni and Cu MOF samples on paper that were synthesised for the same amount of time. In this

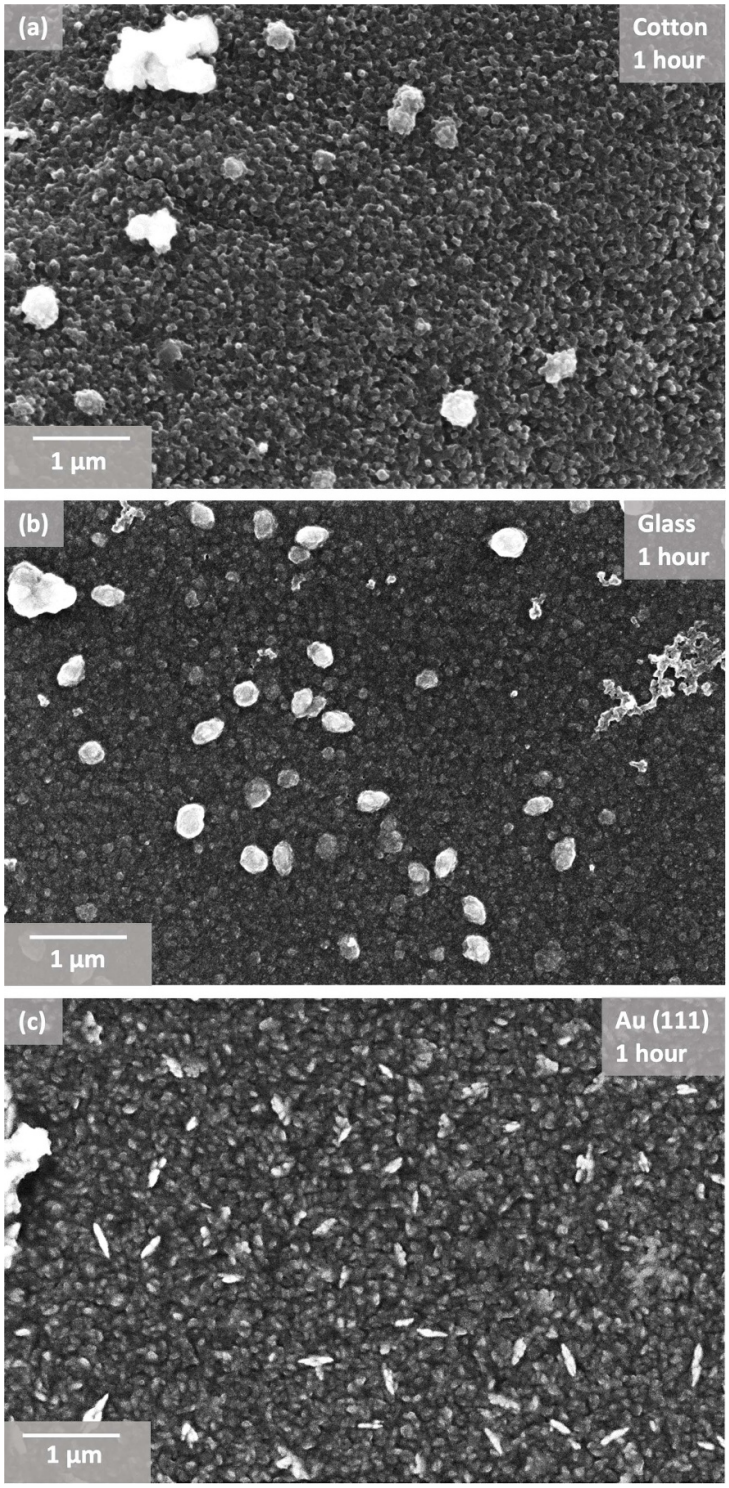

Figure 6. SEM images of $Cu_3(HITP)_2$ MOF synthesised for 1 h on three different substrates: (a) cotton, (b) glass, and (c) Au(111).

figure a lower density of amalgamated MOF crystallites for the $Ni_3(HITP)_2$ image (figure 7(a)) than for the $Cu_3(HITP)_2$ image (figure 7(b)) can be observed. Potential reasons for the slower growth of the Ni MOF than the Cu MOF, despite Ni being the more reactive metal centre, can be ascertained by considering the potential mechanism of MOF formation whereby dissolution of surface metal hydroxide releases M^{2+} ions into the solution for combination with the activated ligand species. The significantly higher solubility of $Cu(OH)_2$ in water than that of $Ni(OH)_2$ could therefore be responsible for the faster rate of Cu MOF formation.

By drawing contacts separated by 0.5 cm onto the paper samples depicted in figure 7 with silver dag, the resistance of the samples could be measured. Prior to submersion of the nanoparticle-decorated paper samples in the MOF synthesis solution, both the Ni and Cu paper samples were insulating. However, after

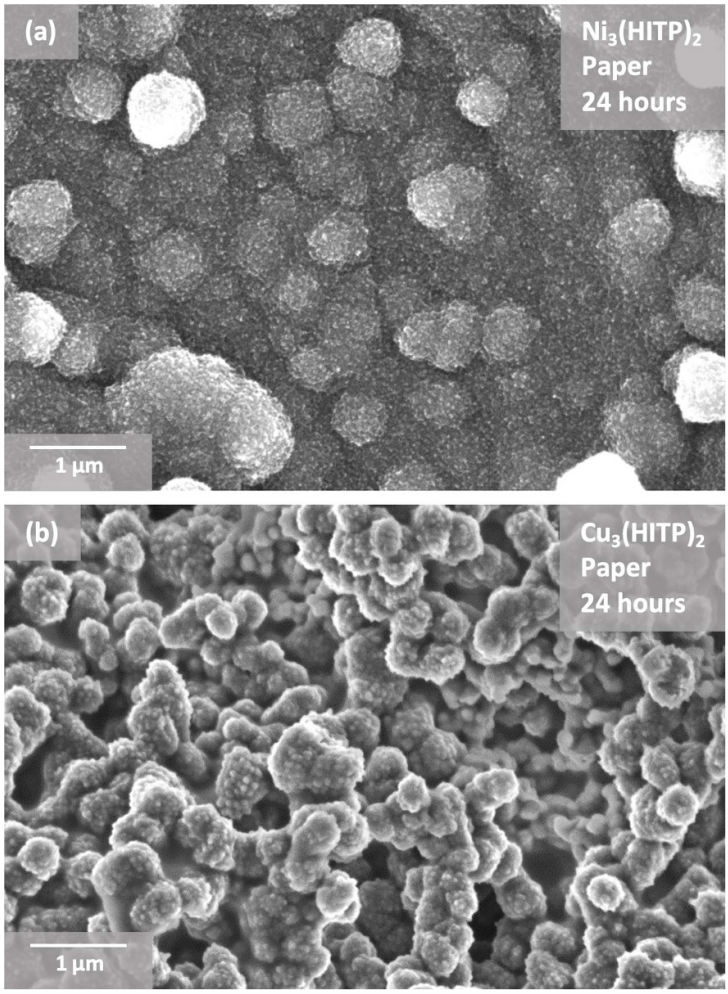

Figure 7. SEM images of (a) $Ni_3(HITP)_2$ and (b) $Cu_3(HITP)_2$ MOF synthesised on paper after 24 h of submersion in the ligand solution.

24 h of submersion in the MOF synthesis solution, the resistance of the $Cu_3(HITP)_2$ sample was measured at 388 kΩ, and the $Ni_3(HITP)_2$ sample at 206 kΩ. The lower resistance of the Ni MOF sample, despite the lower concentration of Ni MOF, reflects the previously-reported higher inherent conductivity of the $Ni_3(HITP)_2$ MOF compared to the $Cu_3(HITP)_2$ MOF [43, 48].

4. Conclusions

A method to synthesise $Cu_3(HITP)_2$ and $Ni_3(HITP)_2$ MOFs *in situ* on a variety of conductive and insulating substrates has been presented. The method uses metal nanoparticles as the metal source to synthesise the MOFs via submersion of the decorated substrates in an alkaline solution of the ligand in the presence of an electrolyte. SEM imaging reveals that the MOF begins to form on the substrate within 10 min of submersion in the ligand solution. By using metal nanoparticles deposited with a magnetron sputtering source, any substrate that fits inside the sputtering chamber can be used. Therefore, this method is expected to be widely applicable to substrates beyond the cotton, glass, paper and gold explored in this work. This method has the potential for use on many substrates as it is salt-free, rapid, and does not require toxic solvents or elevated temperatures. The proven effectiveness of the method in synthesising conductive MOFs *in situ* on IDEs could be employed in the area of chemiresistive sensing, whilst the mild conditions in general make this method promising for direct growth in delicate electronic devices. The ability to synthesise conductive MOFs on flexible insulating substrates such as cotton and paper is significant for the development of flexible and wearable technologies. The next step to advance this research would be to assess the performance of devices that use the MOFs synthesised by our method as the active material. Scaling up the MOF synthesis to cover larger areas should also be investigated.

Data availability statement

All data that support the findings of this study are included within the article (and any supplementary files).

Acknowledgment

We would like to thank the EPSRC for a DTP award (A.M.L.) and an EPSRC-iCASE award with Dstl (B.I.A.). The authors acknowledge use of characterisation facilities within the David Cockayne Centre for Electron Microscopy (DCCEM), Department of Materials, University of Oxford, alongside financial support provided by the Henry Royce Institute (EP/R010145/1). We would also like to thank Sparsh Tyagi for academic discussions, Dr Wai Man from the Oxford Materials Characterisation Service for XPS data acquisition, Dr Neil Young from the DCCEM for TEM imaging, and Srinivasa Rao Saranu from Nikalyte Ltd for assistance with the NL50 cluster deposition system.

Conflict of interest

There are no conflicts to declare.

ORCID iD

Martin R Castell https://orcid.org/0000-0002-4628-1456

References

[1] Sumida K, Rogow D L, Mason J A, McDonald T M, Bloch E D, Herm Z R, Bae T-H and Long J R 2012 *Chem. Rev.* **112** 724
[2] Mahajan S and Lahtinen M 2022 *J. Environ. Chem. Eng.* **10** 108930
[3] Trickett C A, Helal A, Al-Maythalony B A, Yamani Z H, Cordova K E and Yaghi O M 2017 *Nat. Rev. Mater.* **2** 17045
[4] Sher F, Hayward A, El Guerraf A, Wang B, Ziani I, Hrnjić H, Boškailo E, Chupin A and Nemțanu M R 2024 *J. Mater. Chem.* A **12** 27932
[5] Kadhom M and Deng B 2018 *Appl. Mater. Today* **11** 219
[6] Yang F, Du M, Yin K, Qiu Z, Zhao J, Liu C, Zhang G, Gao Y and Pang H 2022 *Small* **18** 2105715
[7] Ahmadijokani F, Molavi H, Rezakazemi M, Tajahmadi S, Bahi A, Ko F, Aminabhavi T M, Li J R and Arjmand M 2022 *Prog. Mater. Sci.* **125** 100904
[8] Connolly B M, Madden D G, Wheatley A E H and Fairen-Jimenez D 2020 *J. Am. Chem. Soc.* **142** 8541
[9] Ahmed A, Seth S, Purewal J, Wong-Foy A G, Veenstra M, Matzger A J and Siegel D J 2019 *Nat. Commun.* **10** 1568
[10] Zhao D, Wang X, Yue L, He Y and Chen B 2022 *Chem. Commun.* **58** 11059
[11] Ahmed S, Shim J, Sun H J and Park G 2020 *Phys. Status Solidi A* **217** 1900969
[12] He Y, Liu W and Liu J 2024 *Colloid Interface Sci.* **661** 409
[13] Ahmed S, Shim J, Sun H-J and Park G 2021 *Surf. Coat. Technol.* **408** 126786
[14] Bajwa R A, Farooq U, Ullah S, Salman M, Haider S and Hussain R 2023 *J. Energy Storage* **72** 108708
[15] Eddaoudi M, Kim J, Rosi N, Vodak D, Wachter J, O'Keeffe M and Yaghi O M 2002 *Science* **295** 469
[16] Hmadeh M *et al* 2012 *Chem. Mater.* **24** 3511
[17] Campbell M G, Liu S F, Swager T M and Dincă M 2015 *J. Am. Chem. Soc.* **137** 13780
[18] Koo W-T, Jang J-S and Kim I-D 2019 *Chem* **5** 1938
[19] Jo Y-M, Jo Y K, Lee J-H, Jang H W, Hwang I-S and Yoo D J 2023 *Adv. Mater.* **35** 2206842
[20] Huang C *et al* 2024 *Angew. Chem. Int. Ed.* **63** e202313591
[21] Clough A J, Yoo J W, Mecklenburg M H and Marinescu S C 2015 *J. Am. Chem. Soc.* **137** 49
[22] Liu L, Xu Q and Zhu Q-L 2021 *Adv. Energy Sustain. Res.* **2** 2100100
[23] Liu K-K, Meng Z, Fang Y and Jiang H-L 2023 *EScience* **3** 100133
[24] Liu J, Song X, Zhang T, Liu S, Wen H and Chen L 2021 *Angew. Chem. Int. Ed.* **60** 5612
[25] Xia W, Mahmood A, Zou R and Xu Q 2015 *Energy Environ. Sci.* **8** 1837
[26] Hong C N, Crom A B, Feldblyum J I and Lukatskaya M R 2023 *Chem* **9** 798
[27] Pereira da Silva C T, Safadi B N, Moisés M P, Meneguin J G, Arroyo P A, Fávaro S L, Girotto E M, Radovanovic E and Rinaldi A W 2016 *Mater. Lett.* **182** 231
[28] Liu X, Zhuo M, Zhang W, Gao M, Liu X-H, Sun B and Wu J 2020 *Ultrason. Sonochem.* **67** 105179
[29] Achmann S, Hagen G, Kita J, Malkowsky I M, Kiener C and Moos R 2009 *Sensors* **9** 1574
[30] Hoppe B *et al* 2018 *CrystEngComm* **20** 6458
[31] Chen X *et al* 2020 *ACS Appl. Mater. Interfaces* **12** 57235
[32] Zhang T, Zheng B, Li L, Song J, Song L and Zhang M 2021 *Appl. Surf. Sci.* **539** 148255
[33] Smith M K, Jensen K E, Pivak P A and Mirica K A 2016 *Chem. Mater.* **28** 5264
[34] Yao M-S, Lv X-J, Fu Z-H, Li W-H, Deng W-H, Wu G-D and Xu G 2017 *Angew. Chem. Int. Ed.* **56** 16510
[35] Smith M K and Mirica K A 2017 *J. Am. Chem. Soc.* **139** 16759
[36] Shu Y, Shang Z, Su T, Zhang S, Lu Q, Xu Q and Hu X 2022 *Analyst* **147** 1440
[37] Zhao Y, Hou N, Wang Y, Fu C, Li X, Li L and Zhang W 2022 *J. Mater. Chem.* A **10** 1248
[38] Zhuang J-LJ.L, Ar D, Yu X-J, Liu J-X and Terfort A 2013 *Adv. Mater.* **25** 4631
[39] De Lourdes Gonzalez-Juarez M, Flores E, Martin-Gonzalez M, Nandhakumar I and Bradshaw D 2020 *J. Mater. Chem.* A **8** 13197
[40] Liu Y, Wei Y, Liu M, Bai Y, Wang X, Shang S, Chen J and Liu Y 2021 *Angew. Chem. Int. Ed.* **60** 2887
[41] Sun C, Wang W, Mu X, Zhang Y, Wang Y, Ma C, Jia Z, Zhu J and Wang C 2022 *ACS Appl. Mater. Interfaces* **14** 54266

[42] Eagleton A M et al 2022 J. Am. Chem. Soc. 144 23297
[43] Sheberla D, Sun L, Blood-Forsythe M A, Leyman Er S, Wade C R, Brozek C K, Alań Aspuru-Guzik A and Dincă M 2014 J. Am. Chem. Soc. 3 8859
[44] Li C, Zhang L, Chen J, Li X, Sun J, Zhu J, Wang X and Fu Y 2021 Nanoscale 13 485
[45] Miner E M, Fukushima T, Sheberla D, Sun L, Surendranath Y and Dincă M 2016 Nat. Commun. 7 10942
[46] Cai D, Lu M, Li L, Cao J, Chen D, Tu H, Li J and Han W 2019 Small 15 1902605
[47] Mu J, Zhong X, Dai W, Pei X, Sun J, Zhang J, Luo W and Zhou W 2022 Molecules 27 2131
[48] Campbell M G, Sheberla D, Liu S F, Swager T M and Dincă M 2015 Angew. Chem. Int. Ed. 54 4349
[49] Li S, Xie L, He M, Hu X, Luo G, Chen C and Zhu Z 2020 Sens. Actuators B 310 127828